Universal Journal of Lasers, Optics, Photonics & Sensors (UJLOPS)
UINUJLOPS202307/W. Arrasmith[1], E. He[2]

Generalizing the Well-Optimized Linear Finder (WOLF) Atmospheric Turbulence Compensation (ATC) Methodology to non-Diversity based Imaging Systems using Entrance Pupil Plane Aperture Masks

W. Arrasmith[1], E. He[2]

[1]Florida Institute of Technology, Melbourne, FL, USA warrasmi@fit.edu, 321-674-8818

[2]Florida Institute of Technology, Melbourne, FL, USA ehe@fit.edu

ABSTRACT

The currently developed Well Optimized Linear Finder (WOLF) atmospheric turbulence compensation (ATC) methodology potentially provides one of the most accurate, fastest, real-time, software-dominant, diversity-based transfer function estimation capabilities available. This has been shown in previous studies through theoretical complexity analysis, computer simulations, and confirmed via experimentation on various laptop computers with different types of Graphical Processor Units (GPUs). At the core of the WOLF algorithm is a unique virtual point method that may be extended, through either hardware or software means, to eliminate the requirement for a directly measured and simultaneously captured diversity image in removing atmospheric turbulence from collected imagery. A hardware approach using entrance pupil plane aperture masks is presented and is directly extendable to hyperspectral imaging systems at desired wavelengths. This can potentially benefit both the spatial resolution aspects of the hyperspectral imaging system, as well as the per pixel signal to noise ratio for spectral data. We present the technical approach, expected results, along with an articulation of the key collection requirements. A speed comparison between this new entrance pupil plane aperture mask approach and previous versions of the WOLF ATC method shows gains of up to 3 orders of magnitude. The WOLF methodology is highly scalable and dramatically benefits from general purpose parallel processing (GPPP) technology such as the GPU on computers, field programmable gated arrays, and/or other GPPP methods.

INTRODUCTION

When imaging through the Earth's atmosphere, optical imaging systems experience loss of spatial resolution due to atmospheric aberrations.[1] The effect of this loss of spatial resolution causes the optical imaging system to fall far short of its diffraction-limited imaging capability, and these atmospheric aberrations can be the limiting factor in the overall optical imaging systems spatial resolution performance, even in well designed optical imaging systems. In order for the atmospheric aberrations to dominate the imaging systems performance, the entrance pupil plane diameter of the optical system must be larger than the atmospheric coherence length ro, known as the Fried parameter.[2] The loss of spatial resolution increases relative to the increase in the entrance pupil plane diameter with respect to the Fried parameter and are present regardless of how well the optical imaging system has been designed. Linear systems theory can often be used to analyze the develop a frequency-space solution to atmospheric turbulence mitigation in optical imagery.[3] To attempt to restore the classical diffraction-limited spatial resolution to the optical imaging system, either Adaptive Optics (AO), Atmospheric Turbulence Compensation (ATC), or a mixture of these two methods (hybrid systems) have traditionally been employed with varying degrees of effectiveness, each with its own pros and cons. For AO systems, these tend to produce real-time atmospheric turbulence corrections (faster than 30 Hz in our definition) but are bulky, hardware intensive, complex, and expensive. They also tend to be more appropriate for fixed sites, can be relatively expensive, and require precision in aligning the optical elements and calibrating the optical system.[1,4] When considering ATC systems, pros consist of being softwaredominant and so can function with very little hardware. However, most ATC systems tend not to be realtime capable and are much slower than AO systems, and so find themselves often used in post-processing applications. The hybrid methods performance-wise lie in between AO and ATC imaging systems and so are less bulky than AO systems but more so than ATC methods. One of the recent ATC methods that is capable of producing real-time, software-dominant ATC for optical imaging system (including hyperspectral imaging systems) known as the Well-Optimized Linear Finder (WOLF) methodology is capable of providing diffraction-limited optical imagery in real-time, but requires a diversity imaging system approach wherein simultaneous image pairs consisting of an in-focus image and a diversity image must be captured as inputs to the WOLF ATC algorithm.[5,6] The diversity image is relatable to the in-focus image and this image pair are the only inputs required by the WOLF methodology to remove the effects of atmospheric turbulence from the captured imagery. In this work, we adapt the WOLF methodology to remove the requirement of the diversity image, so that only a single in-focus image is needed by the WOLF methodology for ATC optical imaging applications. We use a conceptual HSI imaging system layout to illustrate a platform agnostic approach allowing us to focus on the mathematics and methodology without overly emphasizing specific implementation details.

ANALYSIS

When considering a HSI system, the capability of simultaneously capturing spatial information (the image at a given wavelength) and spectral/wavelength information (as a vector of irradiance values at different wavelengths for each spatial pixel) provides the ability to discriminate material characteristics of a scene, at each pixel, and also provide 2D images at differing wavelengths. This provides a powerful capability, for example, to distinguish between natural and man-made artifacts such as tree foliage and camouflage netting. This spatial and wavelength information/data can be provided in numerous ways. Four different notional methods for obtaining HSI data are presented in Figure 1. These methods can be implemented in a variety of different ways.

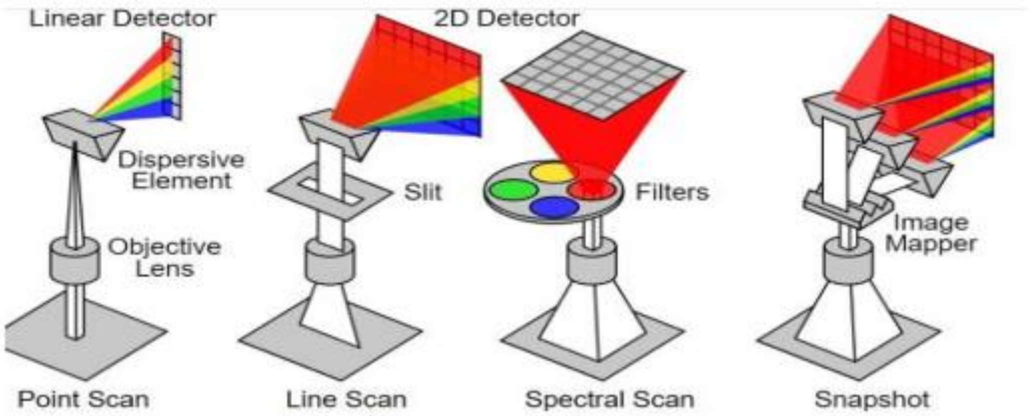

Figure 1 – Various Hyperspectral Imaging system implementation approaches [7]

For the left-most image in Figure 1, this corresponds to a point-scanning mechanism wherein a single pixel is scanned through a 2D scene. A dispersive element such as a prism is used to separate the wavelengths (shown in the vertical, in page direction). The captured image data is then a single spatial pixel of the scene that is split out into its different wavelength components resulting in a vector of image irradiance values, each for the same pixel, but at different wavelengths. The second from the left image in Figure 1 corresponds to a line scanner which acts in a similar fashion to the point scanner just discussed. Instead of having just one pixel though, we have an entire line of pixels that provide spatial information of the scene. For each pixel in the line, all the irradiance values for the pixel at separate wavelengths are simultaneously captured. The third image from the left is a spectral scanner where the entire 2D spatial array is captured at a given wavelength. The 2D spatial response at other wavelengths is obtained by rotating narrow-band filters that are centered at different wavelengths/spectral bands. The last image on the right provides a snapshot of the entire hypercube (both 2D spatial and wavelength information at each pixel) all at once. A diffraction grating is used to separate out lines of pixels, and dedicated prisms are used to split out the wavelengths for each line. There are a variety of other implementation methods to obtain HSI data, and the WOLF ATC method can be made to work with any of them. In all the images in Figure 1, the bottom gray square area represents the 2D spatial plane with x and y coordinates. The four colors shown are representative of the different wavelengths (or spectral bands) but there can be hundreds of wavelengths/spectral bands collected with the HSI system. For our conceptual model, we focus on the linear array of pixels shown in the second from the left image of Figure 1. This operational modality is often referred to as a “push broom” mode wherein the spatial array of pixels is oriented perpendicular to the platform direction of propagation and is pushed in the same direction the platform is moving. Another operational mode for the linear array of spatial pixels is the “whisk broom” mode wherein the pixels are aligned in the direction of propagation of the host platform and subsequently scanned perpendicular to the direction of propagation. As a representative example, we use the line scan mechanism in this paper, shown as the second image in Figure 1, to illustrate our concepts, but our methods can be generalized to any of the HSI implementation approaches. To describe the WOLF ATC methodology that eliminates the requirement for a diversity image term, we must first provide a notional conceptual layout (conceptual model) that captures the general features and attributes of our representative push broom HSI system and provides the necessary image data that is used as inputs to the WOLF ATC algorithm. Figure 2 shows a conceptual layout that provides the required data. Note that Figure 2 is meant to illustrate the adaptations to the WOLF ATC methodology and does not represent a physical optical layout, nor a particular physical implementation of the HSI system itself.

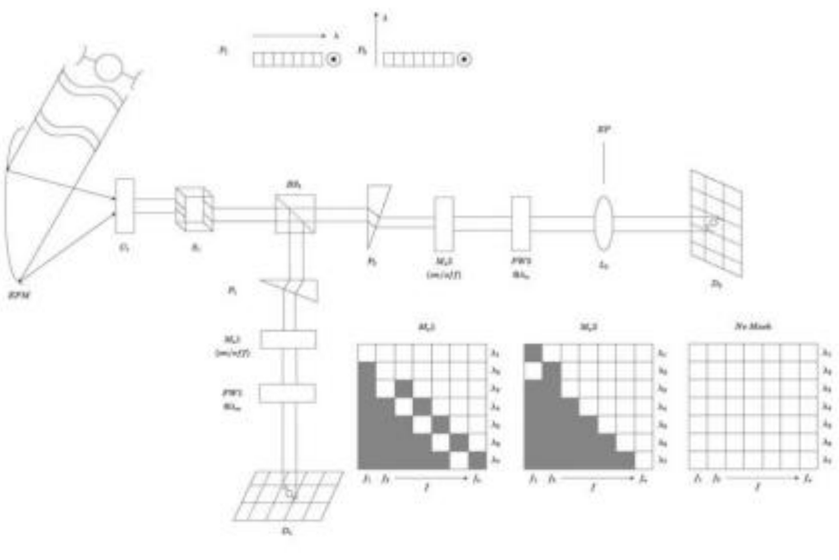

Figure 2 – Conceptual model for non-diversity based HSI system using entrance pupil plane aperture masks.

The conceptual model starts at the top left with an extended object shown as a satellite that has an associated radiant emittance. The object's electromagnetic field propagates through the Earth's atmosphere to a collecting aperture that is assumed to be in the far-field of the object. The collecting aperture is often a primary mirror that lies in the entrance pupil plane of an imaging system. We are assuming a HSI imaging system for this conceptual model. The electromagnetic field is gathered by the entrance pupil plane mirror (EPM) and is focused onto a collimator (C1) which collimates the light into a straight beam. The collimated beam goes through a slit (S1) which selects a linear array of spatial frequencies (shown coming out of the page) along with all the wavelengths for each spatial frequency. The beam of light is split into two separate optical paths, one horizontal that continues to the right after the beam splitter (BS1), and one vertical that continues downwards from the beam splitter. For the horizontal path to the right of the beam splitter, the beam goes through a prism (P2) which separates the wavelengths for each spatial frequency component. The orientation is such that the spatial frequencies (represented by the linear array of square pixels in the top legend) are coming out of the page, as is represented by the circularly enclosed dot. The direction that the wavelengths are separated into are indicated by the arrow next to P2 and shows that they separate in the plane of the page. The separated spatial frequency and wavelength components of the electromagnetic field appear as a 2D array with the spatial frequency components of the electromagnetic field as column elements and the wavelength components associated with the same spatial frequency along the rows of the array. An entrance pupil plane mask (Ma2) that consists of fully blocking cells (shown as black) or fully transmissive cells (shown as white) is then applied to the spatial frequency and wavelength separated array. The patterns of the arrays are shown at the bottom of Figure 1 and can be turned on or off by rotating them in or out of the optical beam path for instance. Other masks could be used but we use these patterns as representative examples that illustrate the concepts for eliminating the diversity image requirement for the WOLF ATC methodology. A selectable filter wheel (FW2) is then applied that can apply a narrow-band filter at any of the wavelengths of the HSI system or let all the wavelengths pass. For example, if the filter wheel is set to $\lambda 1$, then only one row of spatial frequencies components of the electromagnetic field is passed through the filter wheel versus the entire 2D array. The lens (L2) is placed in the exit pupil of the imaging system then takes the 2D Fourier Transform of the filtered light and produces the image in the image plane of the optical system that is detected by detector D2. The image is the 2D Fourier Transform of the point-wise product of the Optical Transfer Function (OTF) at every spatial frequency (which is the autocorrelation of the masked, filtered, and normalized Generalized Pupil Function (GPF)), with the object spectrum. For the downward optical path from the beam splitter, a similar process occurs with the prism (P1) separating out the wavelength components of the optical beam (this time in the horizontal direction, in page) and the spatial frequency still oriented perpendicular to the page. An entrance pupil pane mask (Ma1) and similar filter wheel (FW1) can independently turn the entrance pupil plane mask on or off, and/or apply filters (or not) from the filter wheel. Note that in this conceptual model, we do not show a lens (L1) below filter wheel FW1 indicating that we are measuring the entrance pupil plane brightness values at the detector (D1). By inserting a lens after the filter wheel FW1, we could also measure image plane data if that were desired/beneficial. We will add this to our conceptual model if we need it later. We now present how the WOLF ATC methodology is used in conjunction with the masked entrance pupil plane HSI system to provide ATC imagery at all the HSI wavelengths without requiring a diversity image as in the past. We first focus on describing the entrance pupil plane masks and show how they are useful in generating the optical inputs required by the WOLF ATC algorithm.

A benefit in using this aperture mask is that only a 1-point overlap WOLF algorithm is required for ATC. The 1-point overlap algorithm is much faster than the other WOLF overlap algorithms (i.e., the 2-point overlap and the 3-point (or more) overlap algorithm). By only requiring the 1-point overlap algorithm to remove atmospheric aberrations from imagery, we can gain a significant speed improvement proportional to the number of discrete samples in the phase estimation process. For example, if we had 1000 discrete samples of the entrance pupil plane phase in the range of ($-\pi$, π), we would have a 1000-fold improvement in the ATC speed over the already fast, current WOLF ATC implementation methodology. An additional benefit of using the aperture mask approach is that each spatial frequency row at different wavelengths can be separately and independently processed. In Figure 3, we see the two different aperture masks (Ma1 and Ma2) that are used in our example. The dark areas correspond to the cell entry turned off and so the entrance pupil plane field at that location is set to zero. The white areas correspond to no mask effect and the entrance pupil plane electromagnetic field at those locations are unaffected by the mask. Notice that the orientation of the masks has been shifted with respect to the orientation shown in Figure 2 so that the spatial frequencies for both masks align with the columns and the wavelength separation aligns with the rows. Further, the base row and first wavelength is shown at the top of the array starting with $\lambda 1$. This is to coincide with the matrix representation of MatlabTM which has its first cell at the top left part of the matrix. We find this representation convenient since our WOLF algorithm and many of our image processing functionalities are currently implemented in MatlabTM. The left-most figure shows the mask on the downward leg of the optical path after the beam splitter in Figure 2. The top row is seen to be all clear cells indicating there is no effect of the entrance pupil plane aperture mask at any of the spatial frequency cells associated with $\lambda 1$. Similarly, on the right side of Figure 3 we have the second entrance pupil plane aperture mask Ma2 which is simultaneously applied in the top horizontal path in Figure 2. For the second mask, the first spatial frequency cell element from the left at $\lambda 1$ is zeroed, and so does not contribute to the overall entrance pupil plane masked and filtered electromagnetic field or resulting detector image. We now develop the mathematical framework to show how these entrance pupil plane aperture masks work with the WOLF ATC methodology and show how we can eliminate the need for the diversity image.

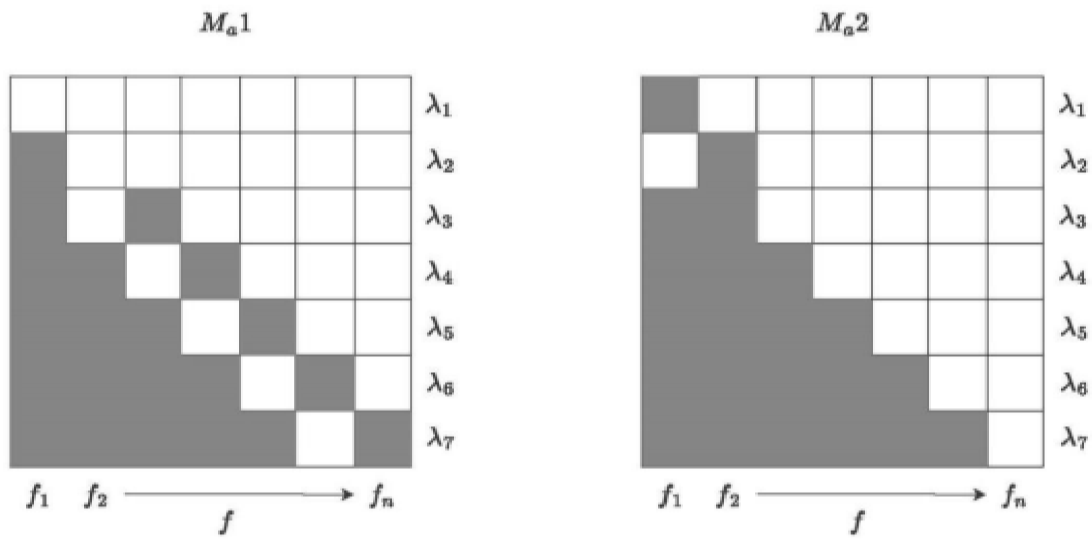

Figure 3 – Entrance pupil plane mask for HSI system.

We have assumed that the entrance pupil of the HSI system is in the far-field of the object, and so can use linear systems theory to rigorously represent the ATC problem and provide a useful mathematical formalism for our conceptual HSI system with our WOLF methodology.[8] For general linear, shift-invariant systems, the image irradiance spectrum at a given wavelength can be related to the object radiant emittance spectrum by,[9]

$$I^{\lambda_n}(\vec{f}) = O^{\lambda_n}(\vec{f})\mathcal{H}^{\lambda_n}(\vec{f}), \tag{1}$$

where $O^{\lambda_n}(\vec{f})$ is the object radiant emittance spectrum at center wavelength λ_n, and spatial frequency $\vec{f} = (f_y, f_x)$, the Optical Transfer Function at the same wavelength and same spatial frequency location is given by $\mathcal{H}^{\lambda_n}(\vec{f})$, and $I^{\lambda_n}(\vec{f})$ is the image irradiance spectrum and is at the same spatial frequency and center wavelength. From Equation (1) we can observe that if we estimate the OTF at the given wavelength and spatial frequency, then we can invert the OTF and determine the atmospheric turbulence free object radiant emittance at that spatial frequency and wavelength. The WOLF methodology is used to estimate the OTF where needed so that the pristine object radiant emittance spectrum can be fully reconstructed. To accomplish this, we first need to express the OTF in terms of entrance pupil plane parameters that we can determine. In Equation (1), we ignore temporal effects and note that the expression only depends on spatial frequency and wavelength parameters. Ignoring temporal effects results from employing Taylor's frozen flow approximation which assumes variations of the atmosphere occur on the scale of milliseconds. Accordingly, to temporally "freeze" the atmospheric state, so that the entrance pupil plane phases properly represent the state of the atmosphere, the integration time on the optical sensor cannot exceed a few milliseconds. The implication with regards to our conceptual optical model is that all the critical measurements needed by the WOLF algorithm need to be made within a few milliseconds. Otherwise, the state of the atmosphere changes and the entrance pupil plane phases determined by the WOLF methodology no longer reflects the correct atmosphere. In our conceptual optical model, if all the spatial frequency data at all wavelengths can be simultaneously captured (such as in a snapshot HSI mode in Figure 1), then the integration times for the detectors D_1 and D_2 should not exceed 1 *ms* each for the masks M_a1 and M_a2 on, and 1 *ms* for these masks turned off. Consequently, only spatial frequency and wavelength information is relevant, and temporal effects can be ignored. The GPF is represented as $W^{\lambda_n}(\vec{f})$ and can be related to the OTF, $\mathcal{H}^{\lambda_n}(\vec{f})$ by,

$$\mathcal{H}^{\lambda_n}(\vec{f}) = \frac{W^{\lambda_n}(\vec{f}) \otimes W^{\lambda_n}(\vec{f})}{N_{ep}}, \tag{2}$$

where the symbol $\otimes$ represents 2D autocorrelation, N_{ep} is the total number of entrance pupil plane sample points of the HSI imaging system at a single wavelength, and the GPF is given by,

$$W^{\lambda_n}(\vec{f}) = A(\vec{f})e^{j\theta^{\lambda_n}(\vec{f})}. \tag{3}$$

In Equation (3), $A\ (\vec{f})$ is an amplitude function that defines the amplitude of the GPF, and is set to one inside the clear aperture of the entrance pupil of the imaging system, and is set to zero outside of the aperture for many imaging systems that operate within the Earth's atmosphere (such as telescopes that are looking up through the atmosphere into space). The amplitude effects become important for distributed turbulence applications, such as ground-to-ground imaging over long paths, or in laser applications where there can be scintillation effects. The parameter $\theta\ (\vec{f})$ in Equation (3) describes the atmospheric aberrations at spatial frequency $\vec{f}$ and at wavelength λn. A common assumption is that phase effects dominate the atmospheric aberrations and so the amplitude value in Equation (3) is set to 1 inside the clear aperture of the entrance pupil and is set to zero outside of the entrance pupil plane aperture. As is common in optical systems analysis, we also initially assume the optical systems transverse and longitudinal magnifications are set to one and address any system magnification effects separately as necessary. At unit magnification, the $\vec{x}o$ coordinate in the object plane has the same scaling as the entrance pupil plane coordinate $\vec{x}p$ and the image plane coordinate $\vec{x}i$, and so we can drop the subscripts and use $\vec{x}$ as the 2D spatial position in any of these planes. Which plane is meant depends on the context of the surrounding discussion. We can also relate the spatial coordinate $\vec{x}$ in the entrance pupil plane to the spatial frequency component in the entrance pupil plane by, $\vec{x} = \lambda n d i \vec{f}$ where di is the imaging system's effective focal length. By looking at Equation (2) we see that the OTF is given by a 2D autocorrelation of the GPF that is normalized by dividing by the total number of entrance pupil planes samples. Usually, determining the OTF in accordance with Equation (2) is tedious and very slow compared to Fourier Transform methods, but there have been several improvements made in the WOLF methodology so that this is no longer the case. Some fundamental improvements in the WOLF methodology include 1) dramatically reducing the number of complex exponential phase difference sum calculations due to the 2D autocorrelation of the GPF to no more than the sum of 2 complex exponentials and a complex constant, instead of possibly millions per OTF point, 2) exploits entrance pupil plane phase redundancies in estimating the OTF, 3) accounts for inherent symmetries in the OTF, 4) can take advantage of parallel processing technology for high-speed parallel calculations, and 5) implements optimization strategies that reduce the computational complexity of the WOLF methodology and maximizes its computational speed. Because of these features, the WOLF methodology has the potential of providing realtime ATC capabilities that are scalable and extendable to HSI imaging systems. In providing the adaptation of the entrance pupil plane aperture mask and filter approach presented in this paper, we can further increase the speed of the WOLF ATC algorithms as will be detailed below.

Equation (2) shows that the masked OTF for the downward optical path in Figure 2 can be determined by a normalized 2D autocorrelation of the GPF formed with the masked entrance pupil plane aperture Ma1. We can see in Figure 4 this specific 2D realization of one point of the OTF obtained be overlapping the last column of the moving, masked entrance pupil plane GPF grid (open dots), so that it overlaps the first row of the fixed GPF grid. The GPF on the moving grid is complex conjugated and then point-wise multiplied with the GPF of the fixed grid, summed together, and then normalized by dividing by the total number of entrance pupil plane samples Nep. This is just a graphical way of carrying out the 2D autocorrelation of the GPF at one spatial frequency point of the OTF. A square aperture is used because any other aperture shape can be created within the bounds of the square by eliminating (setting to zero) certain points at strategic places to provide alternate aperture structural formations. For example, an aperture with the common circular shape can be created by setting points outside of a fixed radius that is centered at the middle of the square aperture to zero. To illustrate the concepts for our WOLF methodology using the entrance pupil plane aperture masks, we use a small 7 x 7 square entrance pupil plane aperture.

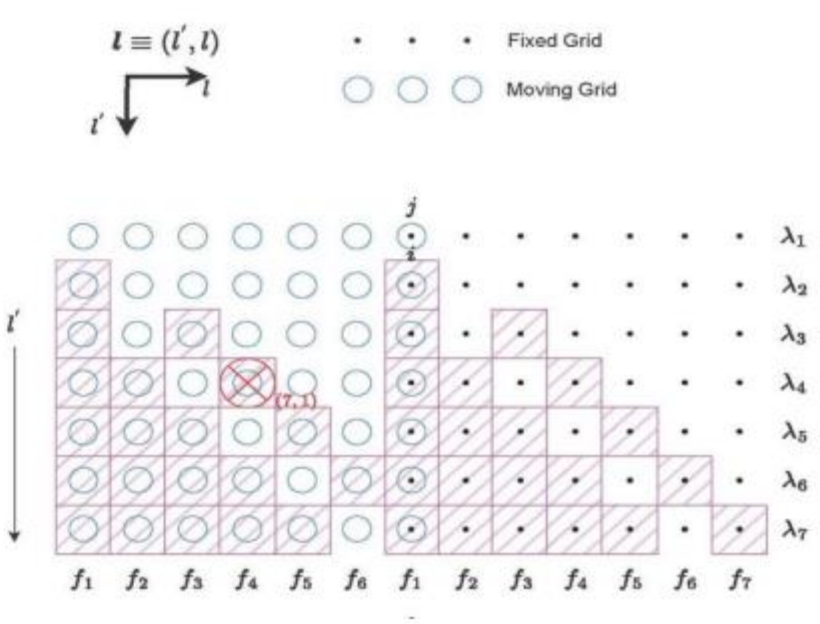

Figure 4 – Optical Transfer Function at spatial frequency coordinate $\boldsymbol{l}$ *= (7, 1 for mask 1 on).*

Our results generalize readily to apertures with larger grid sizes. The first point of our coordinate system for the entrance pupil of our representative push broom HSI system is at the top-left side of the array. The entrance pupil plane phase at this grid location is given by $\theta i\ \lambda 1$ and has units of radians. The last point of the entrance pupil plane phase array at the top right of the fixed array in Figure 4 is given by $\theta j\ \lambda 1$. The progression from left to right of a given rows column entries is given by the set $\boldsymbol{m}\lambda n$ = {1, 2, 3, 4, 5, 6, 7} where for example the first element {1} refers to the first grid point which would be $\theta i\ \lambda 1$ for the entrance pupil plane phase aberrations of the first (top-most) row of Figure 4. Similarly, the last grid index for the n th wavelength would be $m\lambda n$ = {7}. The specific column entry is given by $m\lambda n$ (no bold font) and has a maximum index value of $M\lambda n$ = 7. For the first row with a wavelength of $\lambda 1$, and $m\lambda 1$ index value of {1} we have the left-most point in the horizontal spatial pixel vector that points to the fixed grid coordinate with phase $\theta i\ \lambda 1$ and GPF value of $e\ j\theta i\ \lambda 1$. For the moving array, we can have a similar spatial frequency linear array index given by the set $\boldsymbol{k}\ \lambda n$ that includes the collective indices for the moving array, $\boldsymbol{k}\ \lambda n$ = {1, 2, 3, 4, 5, 6, 7}. For all rows in Figure 4, the left-most point is given by $\theta i\ \lambda n$ and the right-most point by θj . The complex conjugated copy of the fixed array GPF values constitute the shifted, mobile array and so the GPF phase of the mobile grid values are the exact negatives of those of the fixed grid values. An explicit example shows the top, left-most GPF of the moving array given by $e\ -j\theta i\ \lambda 1$, and the top right-most GPF value of the moving array given by $e\ -j\theta j\ \lambda 1$. The OTF is calculated at the center of the moving grid shown by a red circled X and is just the instantiation of the 2D autocorrelation of the GPF, which is the sum of the point-wise product of the fixed array GPF and moving array conjugated GPF components in each overlapping cell, normalized by dividing by the total number of entrance pupil plane samples in the linear array, Nep. Notice that when the entrance pupil plane mask is applied in Figure 4, the overlapping areas that are gray do not contribute to the autocorrelation and are zeroed out. Only the top term in the column of overlapping grids contributes to the OTF resulting in a mathematical representation of the OTF of, $\mathcal{H}\lambda 1\ (l7,\ f1\ ) = e\ j\Delta\theta i,j\ \lambda 1\ /Nep$. We use a grid index of l = (l', l) for the OTF spatial frequencies wherein l' runs in the top to bottom direction (along the direction of changing wavelengths for our example), and l runs from left to right, These indices have maximum values of (L', L). For N distinct wavelengths the push broom HSI system has dimensions of (2N-1, 2M-1). The larger l – grid associated with the spatial frequencies of the OTF then has L’ = 2N-1, and L = 2M-1. If we use Figure 4 as an example, there are 7 spatial frequency pixels in the horizontal direction and 7 different wavelengths in the top-down vertical direction giving dimensions of (13, 13), or 169 unique OTF cell positions in both spatial frequency and wavelength dimensions. In Figure 4, we see that the red X marks where the OTF is being determined and has l coordinates of (7,1). This means that the OTF is being determined in the 7th row and 1st column of the larger l grid. The l = (1,1) OTF coordinate results in a 1-point overlap condition that can be determined by shifting the moving array to the left and upwards as far as it can go, so that there is only a 1-point overlap between the bottom right corner of the moving grid, and the top left corner of the fixed grid. No further shift is possible either leftwards or upwards without disconnecting the moving array from the fixed array and having no overlapping points, resulting in a zero value for the OTF. Notice also that the image irradiance spectrum $I\ \lambda n\ (\vec{f})$ and the object radiant emittance spectrum $O\ (\vec{f})$ are atthe same spatial frequency location as the OTF and so share the l – index grid structure with the OTF. There is now sufficient information and conceptual preparation to understand the benefits of employing an entrance pupil plane mask approach to the WOLF methodology and show how this WOLF adaptation is used to efficiently remove the atmospheric turbulence from collected HSI imagery. If we use the 7 x 7 entrance pupil plane grid structure in Figure 4, we end up with an l – grid that has 13 by 13 cells. If every single OTF point were evaluated, this would require 169 individual cells to fully reconstruct the OTF for all spatial frequencies and wavelengths. An immediate advantage of employing an entrance pupil plane mask such as the one shown on the left side of Figure 3 is that we only need to estimate (M + 1)/2 individual OTF values to fully reconstruct the OTF at all relevant wavelengths. For our 7 x 7 entrance pupil plane example in Figure 4, this results in only 4 required estimates of the OTF instead of the possible 169, a remarkable reduction in computational complexity using the entrance pupil plane mask approach shown in Figure 4. We will now show how the WOLF methodology can be adapted with this entrance pupil plane mask approach to provide these remarkable results.

Using the coordinate system described above, the OTF instantiation in Figure 4 at the l – grid coordinate (7, 1) is given by,

$$\mathcal{H}^{\lambda_1}(l_7', f_1) = e^{j\Delta\theta_{i,j}^{\lambda_1}} / N_{ep}\,. \tag{4}$$

Here the phase difference in the complex exponential is given by $\Delta\theta_{i,j}^{\lambda_1} = \theta_i^{\lambda_1} - \theta_j^{\lambda_1}$, which results from the overlapping GPF (fixed grid) and conjugated GPF (moving grid) at the top and left-most overlapping grid points in Figure 4. From Equation (1), the irradiance spectrum at larger $\boldsymbol{l}$ – grid coordinate (7, 1),

$$I^{\lambda_1}(l_7, f_1) = O^{\lambda_1}(l_7, f_1)\mathcal{H}^{\lambda_1}(l_7, f_1), \tag{5}$$

provides the l' grid location where the wavelength of the moving array and fixed array are the same. The f_1 coordinate corresponds to the first spatial frequency component at the far left of the push broom HSI system. Notice that the $\boldsymbol{l}$ – grid coordinates for the OTF, object radiant emittance spectrum, and image spectrum are all the same and co-located with each other. We can determine the left side of Equation (5) directly by taking the 2D Fourier transform of the detected image at detector D_1 in Figure (2), with the aperture mask on and looking at the irradiance spectrum at the $\boldsymbol{l}$ – grid coordinate (7,1). Since we are using a non-diversity-based ATC imaging system, we can use the second entrance pupil plane aperture mask M_a2 in the horizontal optical path of Figure 2 to get the necessary information needed by the WOLF algorithm to perform ATC using the pair of masked image irradiances. Figure 5 shows the OTF at coordinate (7,1) for the second

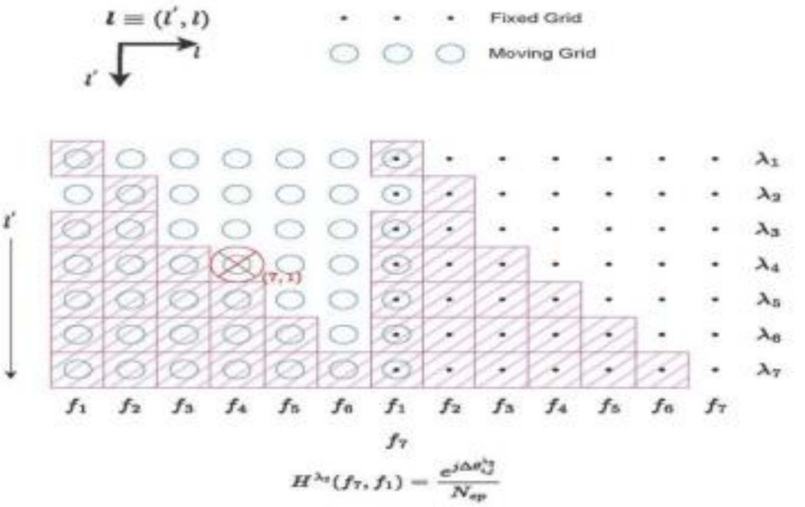

Figure 5 – Optical Transfer Function at spatial frequency coordinate $\boldsymbol{l}$ = (7, 1) for mask 2 on.

mask. Note that this mask isolates the open overlapping pixel in the first column and second wavelength of the fixed and moving entrance pupil plane arrays. For aperture mask Ma2 the filter wheel plays a role in that if it is set to λ2, only the second row of the overlapping fixed and moving grids contribute to the OTF at l- 9 grid coordinate (7,1). For the overlap scenario shown in Figure (5), the mathematical expression for the OTF at λ2 can be expressed as

$$\mathcal{H}^{\lambda_2}(l_7', f_1) = e^{j\Delta\theta_{i,j}^{\lambda_2}} / N_{ep}, \tag{6}$$

where $\Delta\theta_{i,j}^{\lambda_2} = \theta_i^{\lambda_2} - \theta_j^{\lambda_2}$ is like the previous phase difference for Equation (5) but is scaled by the differences in wavelengths. For the irradiance spectrum at λ_2, we get from Equation (1),

$$I^{\lambda_2}\left(l_7', f_1\right) = O\left(l_7', f_1\right) \mathcal{H}^{\lambda_2}\left(l_7', f_1\right), \tag{7}$$

where once again, the left side of Equation (5) can be directly measured from the 2D Fourier Transform of the irradiance measured at detector D_2. At this point, we can make an interesting observation by writing the object spectrum in its phasor form and combining the result with the explicit expressions of the OTFs in Equations (4) and (6). The result is,

$$I^{\lambda_1}(l_7', f_1) = \left|O^{\lambda_1}(l_7', f_1)\right| e^{j\left(\phi_o^{\lambda_1}(l_7', f_1) + \Delta\theta_{i,j}^{\lambda_1}\right)} / N_{ep}\ , \tag{8a}$$

and,

$$I^{\lambda_2}(l_7', f_1) = \left|O^{\lambda_2}(l_7', f_1)\right| e^{j\left(\phi_o^{\lambda_2}(l_7', f_1) + \Delta\theta_{i,j}^{\lambda_2}\right)} / N_{ep}, \tag{8b}$$

where $\phi_o^{\lambda_1}\left(l_7', f_1\right)$ and $\phi_o^{\lambda_2}\left(l_7', f_1\right)$ are the object radiant emittance spectra phase at $\boldsymbol{l}$ – grid coordinate (7, 1). Notice that if we take the absolute value of the measured irradiance spectra at the $\boldsymbol{l}$ – grid coordinate (7,1), then we directly recover the object radiant emittance spectrum magnitudes divided by the known number of entrance pupil sample points, N_{ep}. This interesting feature works for all 1-point overlap scenarios in our approach, and at all wavelengths and is one of the primary reasons for using the entrance pupil plane aperture masks. To proceed, we use the WOLF-Tau, 1-point overlap algorithm to solve for the unknown phase $\theta_j^{\lambda_1}$. We note that $\theta_j^{\lambda_n}$ can be related to $\theta_j^{\lambda_m}$ in general by,

$$\lambda_n \theta_j^{\lambda_n} = \lambda_m \theta_j^{\lambda_m}. \tag{9}$$

To process the WOLF-Tau algorithm, the irradiance spectra in Equations (8a) and (8b) need to be converted to an equivalent 2-point problem by using a virtual point approach that is integral to the WOLF methodology. Equations (8a) and (8b) become,

$$I_2^{\lambda_1}(l_7', f_1) = 2\left|O^{\lambda_1}(l_7', f_1)\right| \cos\left(\tfrac{1}{2}\left(\psi_{i,s}^{\lambda_1} - \psi_{r,j}^{\lambda_1}\right)\right) e^{j\left(\phi_o^{\lambda_1}(l_7', f_1) + \frac{1}{2}\left(\Delta\theta_{i,s}^{\lambda_1} + \Delta\theta_{r,j}^{\lambda_1}\right)\right)} \Big/ N_{ep}\ , \tag{10a}$$

and,

$$I_2^{\lambda_2}(l_7', f_1) = 2\left|O^{\lambda_2}(l_7', f_1)\right| \cos\left(\tfrac{1}{2}\left(\psi_{i,s}^{\lambda_2} - \psi_{r,j}^{\lambda_2}\right)\right) e^{j\left(\phi_o^{\lambda_2}(l_7', f_1) + \frac{1}{2}\left(\Delta\theta_{i,s}^{\lambda_2} + \Delta\theta_{r,j}^{\lambda_2}\right)\right)} \Big/ N_{ep}\ , \tag{10b}$$

where $\psi_{i,s}^{\lambda_1} = \theta_i^{\lambda_1} + \theta_s^{\lambda_1}$, $\psi_{r,j}^{\lambda_1} = \theta_r^{\lambda_1} + \theta_j^{\lambda_1}$, $\psi_{i,s}^{\lambda_2} = \theta_i^{\lambda_2} + \theta_s^{\lambda_2}$, $\psi_{r,j}^{\lambda_2} = \theta_r^{\lambda_2} + \theta_j^{\lambda_2}$, $\Delta\theta_{i,s}^{\lambda_1} = \theta_i^{\lambda_1} - \theta_s^{\lambda_1}$, $\Delta\theta_{r,j}^{\lambda_1} = \theta_r^{\lambda_1} - \theta_j^{\lambda_1}$, $\Delta\theta_{i,s}^{\lambda_2} = \theta_i^{\lambda_2} - \theta_s^{\lambda_2}$, and $\Delta\theta_{r,j}^{\lambda_2} = \theta_r^{\lambda_2} - \theta_j^{\lambda_2}$. We assume a single aperture HSI system with only one primary entrance pupil plane collecting aperture, and so only need to be concerned about relative phase effects, and not absolute phase effects in the imaging system. Therefore, we are free to choose the initial value of $\theta_i^{\lambda_1}$. Note that by converting to an equivalent 2-point overlap problem, the phase information for the OTF has been moved into the magnitude term. The irradiance spectra on the left sides of Equations (10a) and (10b) can be numerically determined from the original 1-point overlap measurements using the virtual point method. We then form the following error metric,

$$E^{\lambda_m,\lambda_n}(\vec{f}) = \left\| \frac{|I^{\lambda_n}(\vec{f})|}{|I^{\lambda_m}(\vec{f})|} - \left| \frac{|O^{\lambda_n}(\vec{f})|}{|O^{\lambda_m}(\vec{f})|} \frac{\cos\left(\frac{1}{2}\left(\psi_{l,s}^{\lambda_n} - \psi_{r,j}^{\lambda_n}\right)\right)}{\cos\left(\frac{1}{2}\left(\psi_{l,s}^{\lambda_m} - \psi_{r,j}^{\lambda_m}\right)\right)} \right| \right\|, \tag{11}$$

where all the parameters are determinable except $\theta_j^{\lambda_n}$ and $\theta_j^{\lambda_m}$, and these phases are relatable to each other through Equation (9) above. Substituting Equations (10a) and (10b) into Equation (11) we get,

$$E^{\lambda_1,\lambda_2}(l_7', f_1) = \left\| \frac{|I_2^{\lambda_2}(l_7', f_1)|}{|I_2^{\lambda_1}(l_7', f_1)|} - \left| \frac{|O_2^{\lambda_2}(l_7', f_1)|}{|O_2^{\lambda_1}(l_7', f_1)|} \frac{\cos\left(\frac{1}{2}\left(\psi_{l,s}^{\lambda_2} - \psi_{r,j}^{\lambda_2}\right)\right)}{\cos\left(\frac{1}{2}\left(\psi_{l,s}^{\lambda_1} - \psi_{r,j}^{\lambda_1}\right)\right)} \right| \right\|, \tag{12}$$

and we only need to search over one cycle of the argument of the cosine term with the shorter wavelength. Assuming that λ_1 is the shorter wavelength, the plot of this error metric, as a function of $\theta_j^{\lambda_1}$ is seen in Figure 6. We see that the error metric $E^{\lambda_1,\lambda_2}(l_7', f_1)$ is a smooth function with one minimum over the principal range

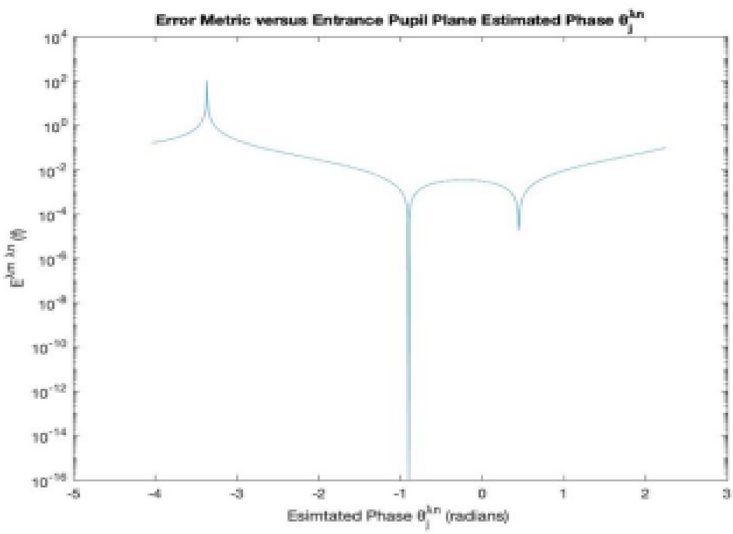

Figure 6 – Error function $E^{\lambda_m,\lambda_n}(\vec{f})$ as function of unknown phase $\theta_j^{\lambda_n}$ over its principal range where (m =1, n=2).

of $\theta_j^{\lambda_1}$. The actual value of the "truth" phase $\theta_j^{\lambda_1}$ was – 0.8976 radians and we see from Figure 6 that the error metric exactly hit the mark. The minimization of this error metric provides the value $\theta_j^{\lambda_1}$ thereby allowing us to determine $\mathcal{H}^{\lambda_1}(l_7', f_1)$ in accordance with Equation (4), and consequently the ATC object spectrum $O^{\lambda_1}(l_7, f_1)$ in accordance with Equation (5). Note also that both $\theta_i^{\lambda_1}$ and $\theta_j^{\lambda_1}$ can be used with Equation (9) to determine $\theta_i^{\lambda_n}$ and $\theta_j^{\lambda_n}$ at any other wavelength in the HSI system for the first and last columns of the entrance pupil. We have effectively determined all the entrance pupil plane phase values for the first and last columns of the entrance pupil plane, across all HSI wavelengths. We can also determine the OTF at any wavelength for the first overlapping column in Figure 5. Notice also that the ATC object spectrum can be recovered at any wavelength by turning off one of the entrance pupil plane masks in Figure 2 and selecting the desired wavelength filter. The image irradiance spectrum is determined from the 2D Fourier transform of the captured image irradiance with the desired wavelength filter in place. The resulting numerical image irradiance spectrum at λn and the OTF for that wavelength can be used to determine the object radiant emittance spectrum for that wavelength. Further, in principle, the object spectra at different wavelengths can be independently and simultaneously determined once $\theta j\ \lambda 1$ has been determined. In practice, this may be more difficult to achieve due to the limited time the atmosphere remains constant.

Next we apply the WOLF methodology to the case where we have two overlapping columns of the entrance pupil plane fixed and moving arrays. We see in Figure 7 the 2 – point overlap scenario wherein the moving array is shifted to the left with respect to the fixed array until the first two columns of the fixed array and last two columns of the moving array overlap. This overlap condition is referred to as the so-called 2- point overlap scenario since only two points of the entrance pupil plane sampled grid overlap at each wavelength. To solve the 2-point overlap at a given wavelength, the WOLF-Iota algorithm is used. We can use the error metric shown in Equations (11) and (12) for the 2-point overlap condition and can directly solve for the needed entrance pupil plane phases.

We can see from Figure 7 that the OTF is now being determined at one horizontal unit to the right of the previous 1-point overlap case and has a new l – grid location (7, 2) that is illustrated by the red X that is inscribed by a red circle. We have four non-zero overlapping cells contributing to the OTF. The overlapping cell that is at the top-left of the first row has the complex exponential phase difference e $\Delta\theta i,\ \lambda 1$ where $\Delta\theta i,\ \lambda 1 = \theta i\ \lambda 1 - \theta s\ \lambda 1$. The complex exponential phase difference term in this top left-most cell is given by the

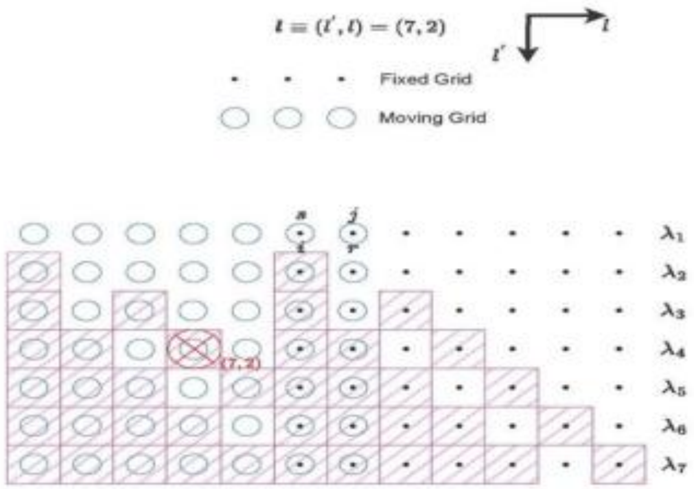

*Figure 7 – Optical Transfer Function at spatial frequency coordinate **l** = (7, 2)* for mask *M_a1*.

point-wise product of the fixed array GPF (shown by dots) with the complex conjugated moving grid GPF (shown by circles). Similarly, in the second cell from the top-left, the OTF component cell entry is given by the fixed array GPF multiplied by the complex conjugated moving array GPF resulting in a cell entry of $e^{\Delta\theta^{\lambda_1}_{r,j}}$ where $\Delta\theta^{\lambda_1}_{r,j} = \theta^{\lambda_1}_r - \theta^{\lambda_1}_j$. For this 2-point overlap in the top row of Figure 7, the values of $\theta^{\lambda_1}_i$ and $\theta^{\lambda_1}_j$ have already been determined from our previous 1-point overlap problem in Figure 4. Therefore, the only two unknowns in the first row of Figure 7 are $\theta^{\lambda_1}_r$ and $\theta^{\lambda_1}_s$. We can use the aperture masks in an interesting way to determine these unknown phases. By looking at the second row of Figure 7, we see that the irradiance spectrum for the λ_2 row of Figure 7 takes on the same form as that for Equation (8b) but with $\theta^{\lambda_1}_i$ in Equation (8b) replaced with $\theta^{\lambda_2}_r$, and $\theta^{\lambda_1}_j$ in Equation (8b) replaced with $\theta^{\lambda_2}_j$. Since we can determine $\theta^{\lambda_2}_j$ from our knowledge of $\theta^{\lambda_1}_j$ and Equation (9), we can use the methods above to solve for $\theta^{\lambda_2}_r$, and Equation (9) can be used to determine the results at any other wavelength. If we now apply the second entrance pupil plane mask M_a*2* in Figure 8, to this 2 – point overlap scenario, we see that applying the filter at wavelength λ_2 produces

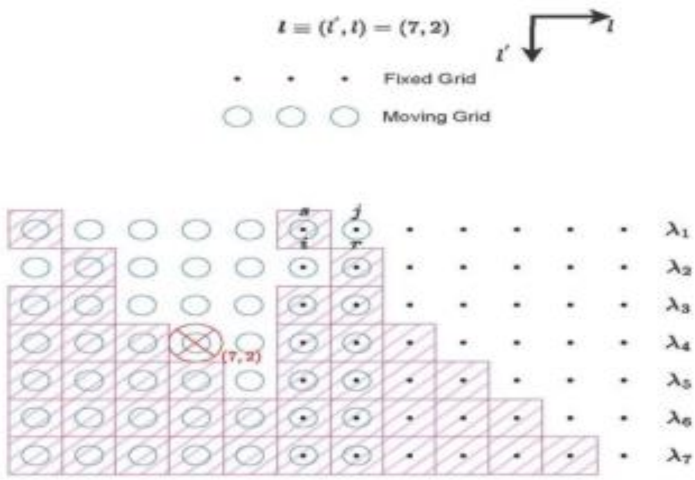

*Figure 8 – Optical Transfer Function at spatial frequency coordinate **l** = (7, 2)* for mask *M_a2*.

the same form of irradiance spectrum as in Equation (8b) but this time with $\theta^{\lambda_1}_i$ in Equation (8b) replaced with $\theta^{\lambda_2}_i$, and $\theta^{\lambda_1}_s$ in Equation (8b) replaced with $\theta^{\lambda_2}_s$. The only difference is that in this case we know $\theta^{\lambda_1}_i$ and $\theta^{\lambda_2}_i$ from the 1-point overlap scenario from before, and so can use the methods detailed above to solve for the unknown phase $\theta^{\lambda_2}_s$, subsequently at all other wavelengths using Equation (9).

When solving for $\theta^{\lambda_2}_r$ using the first aperture mask *M_a1* shown in Figure 7, the 1 – point overlap is converted to a 2 – point overlap equivalent problem and can use the following error metric,

$$E^{\lambda_1,\lambda_2}(l_7',f_2)=\left\|\left|\frac{I_2^{\lambda_2}(l_7',f_2)}{I_2^{\lambda_1}(l_7',f_2)}\right|-\left|\frac{O_2^{\lambda_2}(l_7',f_2)}{O_2^{\lambda_1}(l_7',f_2)}\right|\frac{\cos\left(\frac{1}{2}\left(\psi_{i,s'}^{\lambda_2}-\psi_{r,j}^{\lambda_2}\right)\right)}{\cos\left(\frac{1}{2}\left(\psi_{i,s'}^{\lambda_1}-\psi_{r,j}^{\lambda_1}\right)\right)}\right\|, \tag{13}$$

to find $\theta_r^{\lambda_1}$. Notice that as before, we can determine the irradiance spectrum values from the 2D Fourier Transform of the measured irradiance, and apart from $\theta_r^{\lambda_1}$, the parameters $\psi_{i,s'}^{\lambda_1}$, $\psi_{i,s'}^{\lambda_2}$, $\psi_{r,j}^{\lambda_1}$, and $\psi_{r,j}^{\lambda_1}$ are determinable from the WOLF-Tau virtual point process. Once $\theta_r^{\lambda_1}$ has been determined from the WOLF-Tau algorithm, all phases in the second row of the entrance pupil can be determined from Equation (9). This process can be repeated to solve for $\theta_s^{\lambda_1}$ in the first column of Figure 7 by noting the similarity of the first row of Figure 7, with the filter set to λ_1, with the form of Equation (10a). The only difference is that the irradiance spectrum is given at $\boldsymbol{I}$ – grid coordinate (l_7', f_2) instead of (l_7', f_1) and that the unknown entrance pupil plane phase is $\theta_s^{\lambda_1}$instead of $\theta_j^{\lambda_1}$ in Equation (10a). The second irradiance spectrum expression needed by the error metric can be obtained from Figure 8, with the filter wheel set to λ_2. This irradiance spectrum looks just like Equation (8b) and the same process as for the 1-point overlap can be used to determine the unknown entrance pupil plane phase $\theta_s^{\lambda_1}$. Once $\theta_s^{\lambda_1}$ has been determined, all the other entrance pupil plane phases at the different column elements for the second to the last column in the entrance pupil grid can be determined. Also, the OTF values can be determined at all wavelengths in the HSI system, and the ATC object radiant emittance can be directly determined from Figure 7 by dividing $I2\ \lambda1\ (l7\ '\ ,\ f2\ )$ by $\mathcal{H}2\ \lambda1\ (l7\ '\ ,\ f2\ )$ given by,

$$\mathcal{H}_2^{\lambda_1}(l_7',f_2)=\left(e^{j\Delta\theta_{i,s}^{\lambda_1}}+e^{j\Delta\theta_{r,j}^{\lambda_1}}\right)/N_{ep}. \tag{14}$$

Note that by scaling the individual phases inside the argument of the complex exponential in Equation (14), we can find the OTF for any other wavelength in the HSI system. Also, if we measure the irradiance at any wavelength of interest with either of the masks turned off, we can determine the object radiant emittance at that wavelength by dividing the determined irradiance spectrum at λ_n by the corresponding OTF at the wavelength λ_n. In this manner, just as in the 1-point overlap case, any wavelength for the 2-point overlap case can in principle be corrected. At this point, we have 4 columns of phases determined at all spectral wavelengths of interest. This process can be extended for 3 (or more) point overlap scenarios indefinitely. The generalization of the optical transfer function for the 3 (or more) point overlap scenario case for an arbitrary wavelength λ_n is,

$$\mathcal{H}_k^{\lambda_n}\left(l_{(N_{ep})}, f_{l=k}\right)=\left[\frac{e^{j\left(\Delta\theta_{i,s}^{\lambda_n}\right)}+C_k^{\lambda_n}+e^{j\left(\Delta\theta_{r,j}^{\lambda_n}\right)}}{N_{ep}}\right], \tag{15}$$

where k is the number of overlapping points between the fixed array and moving array at λ_n, the complex constant term $C_k^{\lambda_n}$ is determinable from previous overlap scenarios and changes for each increment of k. In Equation (15), the only unknown entrance pupil plane phases in the OTF expression are $\theta_r^{\lambda_n}$ and $\theta_s^{\lambda_n}$, since $\theta_i^{\lambda_n}$ and $\theta_j^{\lambda_n}$ were obtained from the 1-point overlap method presented above. This OTF expression corresponds to the actual k-point overlap OTF expression with the entrance pupil plane mask turned off at λ_n. Further, the complex constant $C_k^{\lambda_n}$ can be determined by the superposition of complex exponential phase differences that all have been previously determined from prior overlap scenarios. The analytical expression for $C_k^{\lambda_n}$ is given by,[10]

$$C_k^{\lambda_n}=\sum_{p=1}^{k-2}\left[e^{j\left(\theta_{1+p}^{\lambda_n}-\theta_{M-k+1+p}^{\lambda_n}\right)}\right], \tag{16}$$

were k is greater than or equal to 3, and M is the maximum number of entrance pupil plane sample cells in a linear direction (assumed odd so linear samples are symmetric about the center) and at wavelength λn. We just need to find the two unknown phases $\theta r\ \lambda n$ and $\theta s\ \lambda n$ and we can then determine the OTF for any number of overlaps. Using the aperture mask method detailed above, the 3-point (or more) overlap problem can be broken down into two successive 1-point overlap problems that use the almost 3 orders of magnitude faster 1-point WOLF-Tau algorithm. This fast equivalent 1-point overlap conversion is made possible by the employment of the entrance pupil plane masks, and wavelength filter combination. The enabling element is being able to directly estimate the object radiant emittance magnitude from the 1-point overlap analytical expression at selective points of the entrance pupil plane aperture mask. This leaves only two unknown and separated entrance pupil plane phases ($\theta r\ \lambda n$ and θs) in the general error minimization expressions,

$$E_{k;r}^{\lambda_n,\lambda_m}\left(l'_{(N)}, f_k\right) = \left\| \left|\frac{i_k^{\lambda m}(l'_N, f_k)}{i_k^{\lambda n}(l'_N, f_k)}\right| - \left|\frac{\left|o_k^{\lambda m}(l'_N, f_k)\right|}{\left|o_k^{\lambda n}(l'_N, f_k)\right|} \frac{\cos\left(\frac{1}{2}\left(\psi_{l,s'}^{\lambda m} - \psi_{r,j}^{\lambda m}\right)\right)}{\cos\left(\frac{1}{2}\left(\psi_{l,s'}^{\lambda n} - \psi_{r,j}^{\lambda n}\right)\right)}\right| \right\|, \tag{17a}$$

and,

$$E_{k;s}^{\lambda_n,\lambda_m}\left(l'_{(N)}, f_k\right) = \left\| \left|\frac{i_k^{\lambda m}(l'_N, f_k)}{i_k^{\lambda n}(l'_N, f_k)}\right| - \left|\frac{\left|o_k^{\lambda m}(l'_N, f_k)\right|}{\left|o_k^{\lambda n}(l'_N, f_k)\right|} \frac{\cos\left(\frac{1}{2}\left(\psi_{l,s}^{\lambda m} - \psi_{r',j}^{\lambda m}\right)\right)}{\cos\left(\frac{1}{2}\left(\psi_{l,s}^{\lambda n} - \psi_{r',j}^{\lambda n}\right)\right)}\right| \right\|, \tag{17b}$$

where s' and r' are dummy variables that are associated with known entrance pupil plane phases generated by the WOLF-Tau algorithm in minimizing these error equations, N is the maximum number of wavelengths in the HSI system, and the subscripts r and s on the left sides of the equation refer to the phases that are being determined through the error minimization process (i.e., $\theta_r^{\lambda n}$ and $\theta_s^{\lambda n}$ respectively). For each of the error expressions in Equations (16a) and (16b), the unknown phases are broken into discrete estimates across their principal range [$-\pi$, π] and the minimized error provides the best estimate of the actual needed entrance pupil plane phases for the k^{th} entrance pupil plane column (for $\theta_r^{\lambda_n}$) and the $N - k^{th} + 1$ column (for $\theta_s^{\lambda_n}$).

Using the methods presented above, we can make ATC corrections to the HSI push broom sensor imagery at all wavelengths, and the platform motion can be used to map out the 2D image over time t_p. Whatever wavelength filtering that needs to happen for the WOLF methodology to remove the atmospheric aberrations must be accomplished within the time t_p that advances the HSI platform from one row to another. Alternatively, the rows of spatial frequency information can be split out as in the snapshot image mapper shown at the right of Figure 1. If a snapshot image mapper architecture is used, then the requirement for different wavelengths reduces to only two simultaneous wavelengths, greatly expanding the utility of the masked aperture approach and encompassing colored cameras/video and multi-spectral imaging systems. The required image set for the aperture masked WOLF methodology includes irradiance data for the following cases (mask on, filter on; mask off filter on) for each of the required $(N_{ep} + 1)/2$ wavelengths (if spatial/spatial frequency binning methods are not employed), or at two wavelengths if the snapshot image mapper architecture is used. Another option for an arbitrary number of wavelengths is to use the traditional WOLF methodology with the 1-point, 2-point, and 3-point (or more) sub-algorithms to solve for a given row (single wavelength result) and scale the results to whatever wavelengths are needed. This approach requires either the aperture mask is present, or a simultaneously captured diversity image as in the conventional diversity-based imaging systems. For the diversity-based imaging case, no aperture mask is needed and fewer data sets are required (just the irradiance and diversity irradiance at each wavelength) but we would lose the potential speed increase that the entrance pupil plane masks provide (roughly 3 orders of magnitude for 1000 entrance pupil plane sample points). The speed increase stems from only needing the 1 – point overlap WOLF algorithm to solve for all the needed entrance pupil plane phases to determine the OTF. These approaches work on all the HSI implementation shown in Figure 1. As an example of the WOLF ATC algorithm, as would be seen from one wavelength of a HSI system working in the spectral scanning mode of Figure 1 (2nd top-left image), or a normal monochromatic imaging camera, we see in Figure 9 (left) an image of a small structure near the US – Mexican border between San Diego, CA and Tijuana Mexico. On the left side of Figure 9 is a colored reference image as would be generated combining the red, green, and blue

Figure 9 – Reference image of covered structure near US – Mexican border. Courtesy of Sgt. 1st Class Gordon Hyde, Public Domain, https://en.wikipedia.org/wiki/File:Border_USA_Mexico.jpg#filelinks. Right image 256 x256 reference image at one wavelength.

colored spatial images from the spectral sensor to provide a color image, and is equivalent to the image from an RGB camera. On the right side of Figure 9, we see a single wavelength representation of the colored image and the image size has been reduced to 256 by 256 spatial pixels. The reference image on the right is our truth image to which we compare our ATC result. We apply simulated atmospheric turbulence to the reference image at $\lambda 1$ and apply a Von Karman atmospheric turbulence model with a maximum phase variation of 2π radians across the entrance pupil plane aperture, and that has the correct atmospheric turbulence statistics. Figure 10 shows the atmospheric turbulence degraded image for the reference single wavelength HSI image irradiance (left), and the WOLF corrected image on the right side.

Figure 10 – Simulated atmospheric turbulence degraded image irradiance at one wavelength (left), ATC (reconstructed image irradiance using the WOLF methodology (right).

Note that for the atmospheric turbulence degraded image on the left, the structure at the center of the image and the surrounding spatial detail are much blurrier than in the reference image. Note that when comparing the WOLF ATC image to the reference image, the WOLF ATC image restored the spatial detail as in the original image. We used a 127 x 127 sampled entrance pupil plane in our ATC simulation at a specified wavelength. This equates to a minimum required OTF of 253 x 253 pixels which often is rounded up to the next power of 2 in each linear direction (256 x 256) to take advantage of the computational speed of the twodimensional Fast Fourier Transform (2D-FFT). If not spatially separating the individual rows of the HSI hypercube data in the detection process, we need irradiance measurements at 64 distinct narrow-band wavelengths in the HSI sensor and the WOLF-Tau algorithm to perform ATC. We do not require a diversity image if the entrance pupil plane hardware mask is employed. The current WOLF methodology can remove atmospheric turbulence from a 256 x 256 pixel image segment in roughly 9 seconds on conventional laptop computers. [11] By using the aperture mask, we can expect a three order of magnitude computational speed improvement over the existing WOLF implementation. A comparison of the WOLF methodology (with and without the aperture mask) to traditional representative ATC methods is shown in Figure 11. The plot shows the number of elementary operations of the various ATC methods on the logarithmic vertical scale versus the number of camera pixels in a linear direction on the linear horizontal scale.

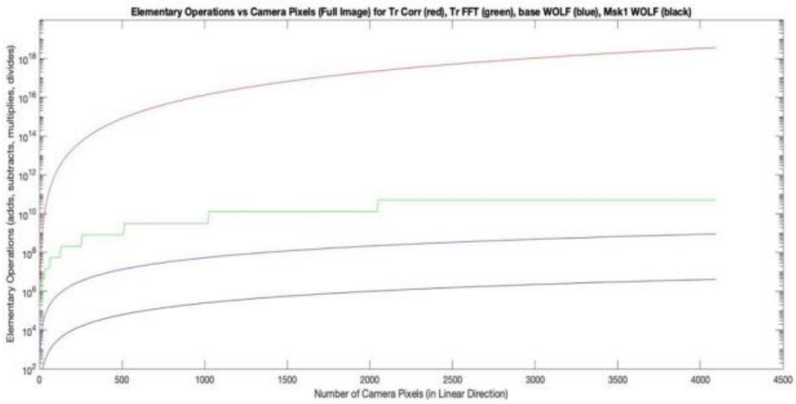

Figure 11 – Number of elementary operations for representative traditional correlation-based ATC methods (top, red), traditional Fourier-based methods (second from top, green), basic WOLF with no optimization or parallelization (third from top, blue), and WOLF method with aperture mask (bottom, black).

At the top of Figure 11, the first line (red) indicates the number of elementary operations (adds, subtracts, multiplies, and divides) of a traditional correlation-based method without any advances or optimizations made in the WOLF methodology. Immediately below, the second (green) line shows the number of elementary operations for a traditional 2D Fourier Transform-based phase diversity implementation. The next line down (blue) is the WOLF methodology without any parallelization, optimizations, or enhancements/adaptations. Note that this conventional WOLF methodology is approximately two orders of magnitude faster than the commonly employed 2D Fourier Transform phase diversity methods. The bottom line (black) shows the expected performance in elementary operations versus camera pixel sizes (in a linear direction) of the WOLF methodology with the entrance pupil plane aperture masks employed. Complexity analysis methods were used to cross check these results, confirmed via simulation over multiple laptop computers dated between 2014 and 2021. [11] All three methods (number of elementary operations, complexity analysis, and simulation) showed good agreement. To capture good quality images that produce notable ATC imagery, some key collection requirements are 1) ensure the diameter of the entrance pupil is (much) larger than the atmospheric coherence length (Fried parameter) ro, ensuring there is sufficient signal (particularly at the edge of the entrance pupil plane aperture, and ensuring there is no aliasing in the object reconstruction process by including proper sampling of the entrance pupil.[12] Satisfying a set of general systems engineering Technical Performance Measures (TPMs) that are tailored to the HSI system is also beneficial.[13]

SUMMARY

We have developed a conceptual framework to apply an adaptation of the WOLF methodology to imaging systems with two (or more) wavelengths. If the rows of the 2D spatial imaging system can be spatially separated so that the row irradiance measurements can be made simultaneously at two different wavelengths, then an entrance pupil plane mask approach can be used to quickly remove atmospheric turbulence from the imagery with an adapted WOLF methodology that is approximately three orders of magnitude faster than the original WOLF ATC approach. If instead, the rows of the imaging sensor cannot be spatially separated so that two different wavelengths can be applied to each row of pixels, then an optical system with many separate, narrow-band wavelengths is necessary. For example, a HSI system with the number of distinct, narrow-band wavelengths equal to or greater than half the entrance pupil plane sample points at a given wavelength can be used in concert with the WOLF methodology to provide atmospheric turbulence compensated hyperspectral imagery. The advantage of using ATC with HSI systems is that the 2D spatial scene at a given wavelength can achieve near diffraction-limited spatial resolution, and the spectral signatures at each pixel will be more accurate allowing for better discrimination of spectral data. This results from the per pixel signal-to-noise ratio at the detector output being increased at all relevant wavelengths. We used a "push broom" HSI architecture to illustrate the entrance pupil plane aperture mask concepts and developed the mathematical formalism for our approach. A conceptual model/layout was presented, and this layout was used to demonstrate the utility of applying the entrance pupil plane masks. The employment of the entrance pupil plane masks produces a three order of magnitude speed increase over the conventional WOLF ATC implementation which would allow for a 256 x 256 image segment to be corrected at one wavelength in roughly 9 ms (barring data I/O and computer memory issues).[11] Once corrected at one wavelength, the entrance pupil plane phase corrections can be immediately scaled to other wavelengths by a single vector multiply. The 9 ms correction time does not include the use of parallel processing technology or any other optimizations and only reflects the effect of introducing the entrance pupil plane aperture mask approach. To gain this edge in processing speed, the hardware complexity of the sensor is increased by adding two entrance pupil plane aperture masks, and narrow-band filter wheels that can be independently turned off or on. In its current configuration, the WOLF methodology can be applied to any of the implementation architectures shown in Figure 1 and does not require the extra hardware of the entrance pupil plane masks. However, the current configuration, without the aperture mask approach presented in this work, does require the simultaneous capture of a diversity image, and so still has some light hardware requirements. Besides requiring the simultaneous capture of the diversity image, another disadvantage of the current WOLF methodology without the entrance pupil plane mask would be the loss of the 3 order of magnitude computational speed advantage that the WOLF implementation with the entrance pupil plane mask provides. The computational speed improvement stems from only requiring the 1 – point overlap algorithm from the WOLF methodology which is ns times faster than the 2 – point, or 3 – point (or more) WOLF algorithms, where ns is the number of entrance pupil plane phase estimate samples passed to the error minimization module in the WOLF methodology (for ns = 1000 entrance pupil plane phase samples, the 1 – point overlap is 1000 times faster than the 2 – point and 3 – point overlap algorithms).

REFERENCES

1. M. C. Roggemann, B. Welsh, Imaging Through Turbulence, CRC Press, New York, 1996
2. Fried, David L. "Statistics of a geometric representation of wave front distortion." JoSA 55.11 (1965): 1427- 1435.
3. J.W. Goodman, Introduction to Fourier Optics, McGraw-Hill, New York, 1968.
4. Paxman, R. G., Seldin, J. H., & Gosselin, K. M. (1992). Atmospheric-turbulence compensation by stochastic parallel gradient descent adaptive optics. Journal of the Optical Society of America A, 9(11), 1969-1986
5. William W Arrasmith. High-speed diversity-based imaging method for parallel atmospheric turbulence compensation, May 21 2013. US Patent 8,447,129.
6. W. Arrasmith. "Diversity-based atmospheric turbulence compensation for incoherent imaging systems using a new well optimized linear finder methodology," Universal Journal of Lasers, Optics, Photonics & Sensors, Vol. 2 Issue No. 1 – June 2021.
7. Wikimedia Commons. (2023). Multispectral Imaging Approaches. svg. Retrieved April 30, 2023,from https://commons.wikimedia.org/wiki/File:Multispectral_imaging_approaches.svg
8. Gaskill, Jack D. Linear systems, Fourier transforms, and optics. Vol. 56. John Wiley & Sons, 1978.
9. Goodman, Joseph W. Introduction to Fourier optics. Roberts and Company publishers, 2005.
10. Erlin He, William W. Arrasmith, and Yang Xin. "Well Optimized Linear Finder (WOLF) Atmospheric Turbulence Compensation (ATC) computational speed improvement through the adoption of parallel, precalculated constant complex exponential phase difference chains," Universal Journal of Lasers, Optics, Photonics & Sensors, Vol. 2 Issue No. 1 – June 2021.
11. Xin, Yang, William W. Arrasmith, and Erlin He. "Order analysis comparison between traditional Fourier transform-based atmospheric turbulence compensation methods and new well optimized linear finder methodology," Universal Journal of Lasers, Optics, Photonics & Sensors, Vol. 2 Issue No. 1 – June 2021.
12. Beckers, Jacques M. "Adaptive optics for astronomy: principles, performance, and applications." Annual review of astronomy and astrophysics 31.1 (1993): 13-62
13. Arrasmith, William Wolfgang. Systems engineering and analysis of electro-optical and infrared systems. CRC Press, 2018